AIAA Paper 2004-0199

# Numerical Study on Flow Separation of A Transonic Cascade

Zongjun Hu* and GeCheng Zha†
Dept. of Mechanical Engineering
University of Miami
Coral Gables, FL 33124
Email: zha@apollo.eng.miami.edu

Jan Lepicovsky‡
QSS Group, Inc.
NASA Glenn Research Center
21000 Brookpark Road
MS 500/QSS
Cleveland, Ohio 44135

## Abstract

The 3D compressible *Navier-Stokes* equations with *Baldwin-Lomax* turbulence model are solved to study the flow separation phenomenon in a NASA Transonic Flutter Cascade. The influence of the incidence angle and the inlet Mach number on the flow pattern in the cascade is numerically studied. When the incoming flow is subsonic, increasing the incidence angle generates a large separation region starting from the leading edge on the suction surface. Higher subsonic inlet Mach number results in a larger separation region. The separation region shrinks and moves downstream when the inlet Mach number is increased to supersonic due to the shock wave boundary layer interaction.

## 1 Introduction

The trend in the design of advanced transonic fans for aircraft engines is to use low-aspect-ratio blades with higher loading. However, this also results in an increased possibility of transonic fans to operate within the region of stall flutter and suffer high cycle fatigue (HCF). Flutter is one of the major design considerations in designing advanced aircraft engines. It is essential to understand the origins and mechanism of flutter to achieve reliable and safe operation of these engines.

Flutter is a self-excited mode of blade oscillation. In almost all cases, flutter is characterized by very sharp drops in stability for relatively small changes in speed. High subsonic and transonic torsional stall flutter occurs near the fan stall limit line at speeds up to about 80% of the design speed and with high incidence. It has often been considered that flow separation is an essential part of the mechanism to induce flutter, and the blade oscillations are triggered by high frequency aerodynamic forcing variation in the separated area on the airfoil suction side.

The NASA Glenn Research Center (GRC) has carried out a series of cascade wind tunnel tests to provide the data for blade flutter research. An extensive experimental study on the nature of the separated flows of a modern transonic fan airfoil at high incidence has been reported[7]. In their research, visualization methods were used to investigate the flow separation. Steady and unsteady pressure measurement was carried out to quantify the unsteady aerodynamic forcing[6].

In this paper, the time-dependent 3D *Navier-Stokes* equations with *Baldwin-Lomax* turbulence model are solved to study the separation phenomenon in the NASA transonic flutter cascade[5]. The flow field is calculated as steady state.

In the following sections, the details of the numerical method are introduced first. Then the code is validated with

* PhD student,
† Associate Professor, AIAA Member
‡ Senior Research Supervisor, AIAA Member

the turbulent flat plate boundary layer flow and a transonic inlet-diffuser flow. The 3D simulation is carried out for the cascade at different incidence (0° and 10°) and different inlet Mach numbers (0.5, 0.8 and 1.18).

# 2 Numerical Algorithms

## 2.1 Governing Equations

The governing equations are the 3D *Reynolds* averaged time-dependent compressible *Navier-Stokes* equations in generalized coordinate system. For simplicity, the non-dimensional form of the equations in conservation law form are expressed in Cartesian coordinates as the following.

$$\frac{\partial \boldsymbol{Q}}{\partial t} + \frac{\partial \boldsymbol{E}}{\partial x} + \frac{\partial \boldsymbol{F}}{\partial y} + \frac{\partial \boldsymbol{G}}{\partial z} = \frac{\partial \boldsymbol{R}}{\partial x} + \frac{\partial \boldsymbol{S}}{\partial y} + \frac{\partial \boldsymbol{T}}{\partial z} \quad (1)$$

where

$$\boldsymbol{Q} = [\bar{\rho}, \bar{\rho}\tilde{u}, \bar{\rho}\tilde{v}, \bar{\rho}\tilde{w}, \bar{\rho}\tilde{e}]^T$$

$$\boldsymbol{E} = [\bar{\rho}\tilde{u}, \tilde{p} + \bar{\rho}\tilde{u}^2, \bar{\rho}\tilde{u}\tilde{v}, \bar{\rho}\tilde{u}\tilde{w}, (\bar{\rho}\tilde{e} + \tilde{p})\tilde{u}]^T$$

$$\boldsymbol{F} = [\bar{\rho}\tilde{v}, \bar{\rho}\tilde{u}\tilde{v}, \tilde{p} + \bar{\rho}\tilde{v}^2, \bar{\rho}\tilde{v}\tilde{w}, (\bar{\rho}\tilde{e} + \tilde{p})\tilde{v}]^T$$

$$\boldsymbol{G} = [\bar{\rho}\tilde{w}, \bar{\rho}\tilde{u}\tilde{w}, \bar{\rho}\tilde{v}\tilde{w}, \tilde{p} + \bar{\rho}\tilde{w}^2, (\bar{\rho}\tilde{e} + \tilde{p})\tilde{w}]^T$$

$$\boldsymbol{R} = \frac{1}{Re}[0, \bar{\tau}_{xx}, \bar{\tau}_{xy}, \bar{\tau}_{xz}, \beta_x]^T$$

$$\boldsymbol{S} = \frac{1}{Re}[0, \bar{\tau}_{xy}, \bar{\tau}_{yy}, \bar{\tau}_{yz}, \beta_y]^T$$

$$\boldsymbol{T} = \frac{1}{Re}[0, \bar{\tau}_{xz}, \bar{\tau}_{yz}, \bar{\tau}_{zz}, \beta_z]^T$$

shear stresses are expressed as,

$$\bar{\tau}_{ij} = -\frac{2}{3}(\tilde{\mu} + \mu_t)\frac{\partial \tilde{u}_k}{\partial x_k}\delta_{ij} + (\tilde{\mu} + \mu_t)\left(\frac{\partial \tilde{u}_i}{\partial x_j} + \frac{\partial \tilde{u}_j}{\partial x_i}\right)$$

$\beta_x, \beta_y,$ and $\beta_z$ are expressed as,

$$\beta_i = (\tilde{\mu} + \mu_t)\tilde{u}_j\tau_{ij} + \frac{1}{\gamma - 1}\left(\frac{\tilde{\mu}}{Pr} + \frac{\mu_t}{Pr_t}\right)\frac{\partial \tilde{a}^2}{\partial x_i}$$

In above equations, $\rho$ is the density, $u,\ v,\ w$ are the Cartesian velocity components in $x,\ y,\ z$ directions, $p$ is the static pressure, and $e$ is the energy per unit mass, $a$ is the local speed of sound. The overbar denotes a *Reynolds* average, and the tilde is used to denote the *Favre* mass average. The molecular viscosity $\mu$ is determined by the *Sutherland* law. The *Reynolds* stresses are related to mean flow variables through a turbulent viscosity $\mu_t$ based on *Boussinesq* assumption, and the turbulent viscosity $\mu_t$ is determined by the *Baldwin-Lomax* model[1].

## 2.2 Discretization Method

The governing equations (1) are discretized and solved using finite volume method. The equations are rewritten as,

$$\frac{\partial \boldsymbol{Q}}{\partial t} = -\frac{\partial (\boldsymbol{E} - \boldsymbol{R})}{\partial x} - \frac{\partial (\boldsymbol{F} - \boldsymbol{S})}{\partial y} - \frac{\partial (\boldsymbol{G} - \boldsymbol{T})}{\partial z} \quad (2)$$

Using finite volume method,

$$\frac{\partial \boldsymbol{Q}}{\partial t} \cdot \mathrm{d}V = -\int_s \boldsymbol{R}_F \cdot \mathrm{d}\boldsymbol{s}$$

where, $\mathrm{d}V$ is the volume of the control volume cell, $\boldsymbol{s}$ is the cell interface area vector in the normal outward pointing direction, and,

$$\boldsymbol{R}_F = (\boldsymbol{E} - \boldsymbol{R})\,\boldsymbol{i} + (\boldsymbol{F} - \boldsymbol{S})\,\boldsymbol{j} + (\boldsymbol{G} - \boldsymbol{T})\,\boldsymbol{k}$$

Discretize this equation in implicit form with 1st order time differencing. The discretized equations at cell $(i, j, k)$ are written as the following,

$$\begin{aligned} \Delta\boldsymbol{Q} + A^+\Delta\boldsymbol{Q}_{i-1} + A\Delta\boldsymbol{Q} + A^-\Delta\boldsymbol{Q}_{i+1} \\ +B^+\Delta\boldsymbol{Q}_{j-1} + B\Delta\boldsymbol{Q} + B^-\Delta\boldsymbol{Q}_{j+1} \\ +C^+\Delta\boldsymbol{Q}_{k-1} + C\Delta\boldsymbol{Q} + C^-\Delta\boldsymbol{Q}_{k+1} \quad = \quad \boldsymbol{R} \end{aligned} \quad (3)$$

where,

$$\boldsymbol{R} = \frac{\Delta t}{\mathrm{d}V}\left(-\int_s \boldsymbol{R}_F \cdot \mathrm{d}\boldsymbol{s}\right)^n$$

$$\Delta\boldsymbol{Q} = \boldsymbol{Q}^{n+1} - \boldsymbol{Q}^n$$

where, $n$, $n+1$ denote two sequential time steps.

Equation (3) is solved using the line *Gauss-Seidel* iteration method to reach the steady state solutions. Two alternating direction sweeps are carried out in each time step. The convective fluxes $\boldsymbol{E}$, $\boldsymbol{F}$, $\boldsymbol{G}$ are evaluated by *Roe* scheme[8] or *van Leer* scheme[9] with *MUSCL* differencing[4]. Third order differencing is used for convective terms $\boldsymbol{E}$, $\boldsymbol{F}$, $\boldsymbol{G}$ and second order central differencing is used for the viscous terms $\boldsymbol{R}$, $\boldsymbol{S}$, $\boldsymbol{T}$. Local time step is applied to speed up the convergence.

# 3 Results and Discussion

## 3.1 Code Validation

The code has been validated with the *turbulent flat plate boundary flow* and a *transonic inlet-diffuser flow* before it is applied to simulate the cascade separation flow. These two cases are computed as 2D flows. The control volume inter surface inviscid flux is calculated using the *Roe* scheme. The boundary conditions are set up for the two cases in a similar way. The total temperature, total pressure and flow

angle (0° ) are given at the inlet boundary and the static pressure is fixed at the outlet boundary. The wall boundary is treated as adiabatic and no slip wall. For the turbulent flat plate boundary layer flow, the zero gradient boundary condition is applied on the free stream boundary, which is parallel to the wall.

#### 3.1.1 Turbulent Boundary Layer Flow

The performance of the *Baldwin-Lomax* turbulence model is validated with computing a flat plate turbulent boundary layer flow. The mesh is distributed as 80 points uniformly allocated along the wall surface and 60 points allocated normal to the wall surface with a stretch factor of 1.1. The $y^+$ of the first cell center to the wall is kept under 0.2. The *Reynolds* number is $4\times10^6$. The inlet *Mach* number is 0.5. When applying the *Gauss-Seidel* line relaxation method, the *CFL* number is set to be 100. The computed result is compared very well with the *Law of the Wall* as shown in Fig. 1.

#### 3.1.2 Transonic Inlet-Diffuser Flow

The second validation case is a transonic inlet-diffuser flow, which is tested in [2]. Fig. 2 is the mesh used for the calculation. The mesh size is 100×60. The mesh is uniformly distributed horizontally, except that a refinement is applied in the throat region, where a normal shock interacts with the turbulent boundary layer. The mesh is clustered close to upper and lower walls vertically with a stretch factor of 1.1. The maximum $y^+$ of the first cell center close to the wall is below 3. The *Reynolds* number is $4.34\times10^5$ based on the inlet height. The inlet *Mach* number in the computation result is 0.45. At the outlet, the static pressure is fixed as $p_{outlet}/p_t$=0.83. A CFL of 5 is used in the *Gauss-Seidel* iterations.

Figure 3 shows the computed *Mach* number contours, where the shock wave is clearly captured. The upper wall static pressure distribution is compared with the experimental data in Fig. 4. A very good agreement is achieved.

### 3.2 3D Cascade Geometry, Meshing and Boundary Conditions

The test section of the NASA transonic flutter cascade facility is shown in Fig. 5. The test section has a rectangular cross section of 5.84 cm wide (pitch $s$) by 9.59 cm high (height $h$). The aerodynamic chord $c$ is 8.89 cm with a maximum thickness of $0.048c$ at $0.625c$ from the leading edge. This results in a solidity $c/s$ of 1.52. The experimental blades have constant cross section in span-wise direction, except near the end walls, where they have large, diamond-shaped fillets to support the attachment shafts. The blades are not exactly symmetric about the mid-span plane. The fillet on the drive-side is larger than the one on the free side. This makes the full 3D calculation necessary. The three dimensional mesh structure is shown in Fig. 6.

The end walls are located at the bottom and the top. The mesh size is 100 (streamwise)×60 (pitchwise)×60 (spanwise). In the streamwise direction, there are 15, 70 and 15 mesh points allocated upstream, on and downstream of the blade surface. Fig. 7 shows the the blade geometry and the mesh structure at bottom, mid-span and top planes. The mesh is clustered in the area close to the blade surface on the pitch direction and in the area close to the top and the bottom end walls in the spanwise direction. In the streamwise direction, the mesh is clustered in the area close to the leading and trailing edges of the blade, where the flow structure is complicated. The maximum $y^+$ at all wall boundaries is under 3. For clarity, every one of two grid lines is plotted in Fig. 6 and Fig. 7.

The inlet and outlet of the computational domain are located at 1.2 chord upstream and downstream of the blade leading edge and trailing edge. No-slip adiabatic boundary condition is applied on the blade surfaces and on the top, bottom end walls. The inlet and outlet boundary conditions vary with the local *Mach* number. At the inlet, if the flow is supersonic, all parameters, including the total pressure $P_t$, total temperature $T_t$, the streamwise velocity and the flow angles $\alpha$, $\beta$ are given at the inlet boundary. If the inlet flow is subsonic, the velocity is extrapolated from the inner domain. At the outlet boundary, if the flow is supersonic, all parameters are extrapolated from upstream to the boundary with zero gradient. If the flow is subsonic, a constant static pressure $p_{outlet}$ is given. In the pitch direction, the periodical boundary condition is applied on the boundaries upstream and downstream of the blade surfaces.

The incidence angle and the inlet Mach number are the two important factors to determine the flow separation pattern in the cascade. In the following simulations, the cases with the incidence angle of 0° and 10°, and the inlet *Mach* number of 0.5, 0.8 and 1.18 are computed and compared with the experimental results. As suggested in [3], the flow incidence angle ahead of the blade will not exactly follow the chordal incidence angle. The incidence uncertainty in the experiment is about 1.5°. Therefore, the incidence angle is adjusted for each case in the computation based on the experiment results. During the process of the *Gauss-Seidel* iterations, a smaller CFL number of 1.0 is used in the first 50 steps and then a higher CFL number of 5.0 is used for the rest computation. For the 3D cascade simulation, the *van Leer* scheme instead of the *Roe* scheme is used to evaluate the inviscid flux. The *Roe* scheme predicts the separation region significantly larger than that in the experiment.

### 3.3 Cascade flow without separation

Before studying the high incidence angle cases, the zero incidence angle case is computed to validate the code in 3D

conditions. In the calculation, the flow incidence is set as 2.5° for the case of incidence 0° in the experiment due to the experimental uncertainty. The inlet *Mach* number of 0.5 is achieved by adjusting the back pressure at the outlet. The *Reynolds* number based on the chord length *c* is $9.6699 \times 10^5$.

Figure 8 shows computed mid-span stream lines at incidence angle 0°. The flow goes through the cascade passage smoothly with no separation. The distribution of the computed static pressure coefficients, $C_p = \frac{p - p_{in}}{\frac{1}{2}\rho_{in} U_{in}^2}$, at the mid-span plane is shown in Fig. 9, which is in good agreement with the experiment. In the $C_p$ formulation, $p$ is the local static pressure, $p_{in}$, $\rho_{in}$ and $U_{in}$ are the averaged static pressure, density and velocity at the inlet.

## 3.4 Cascade flow with separation

The flow is separated when the incidence is increased. The characteristics of the separation varies with the inlet *Mach* number. *Mach* numbers of 0.5, 0.8 and 1.18 are chosen for calculation since the corresponding experimental measurement results are available for comparison. The experimental incidence angle of 10° is used for all the calculations below.

### 3.4.1 M = 0.5

The stream lines on the mid-span plane with inlet *Mach* number 0.5 is shown in Fig. 10 (a). It differs from the low incidence angle case (Fig. 8) with a large flow separation area on the suction surface, which starts immediately at the leading edge and extends down to 45% of the blade chord. The computed and measured flow patterns from the bottom wall (left) to the top wall (right) on the suction surface are plotted in Fig. 11. The experimental flow pattern is obtained with the dye oil technique. The computation shows the similar flow pattern as measured in the experiment. The computed separation bubble length in the midspan location agrees very well with the experiment, but the computed separation area is fuller in the span-wise direction. This indicates that the computed end wall boundary layer is thiner than that in the experiment. This may be because that the computational domain has shorter end wall length than the wind tunnel in the experiment.

The computed separation region has a parabola shape, which is approximately symmetric about the blade mid-span plane. Two counter rotating vortexes are formed downstream of the blade leading edge and end wall corners.

The mid-span surface static pressure distribution is plotted and compared with the experiment measurement in Fig. 14. The pressure on the pressure surface agrees fairly well with the experiment. In the area of the suction side leading edge, the computed pressure rises more steeply than that of the measurement. The separation bubble length represented by the cross of the surface pressure distribution on the suction and the pressure surface is predicted accurately compared with the experiment.

### 3.4.2 M = 0.8

At the inlet *Mach* number of 0.8, the separation exhibits the similar pattern to that in the case of Mach number 0.5. However, the size of the separation region increases significantly. As shown in the computed stream lines in Fig. 10 (b), the separation bubble is larger in both streamwise and pitchwise directions on the midspan plane. The separation region on the suction surface becomes as long as 60% of the chord length. The growth of the separation is also clearly shown in the suction surface flow pattern in Fig. 12. The separation length is a little longer than the corresponding experiment visualization result on the mid-span plane and fuller in the spanwise direction. The asymmetry of the flow pattern due to the asymmetric geometry is more clearly seen in Fig. 12.

The mid-span surface static pressure is plotted and compared with the measurement in Fig. 15. Similar to the case of M=0.5, the computed surface pressure agrees very well on the pressure side. The main difference remains in the leading edge region of the suction surface with the computed surface pressure rising too rapidly. Again, the separation bubble length is predicted fairly well compared with the experiment.

### 3.4.3 M = 1.18

For the supersonic incoming flow with Mach number 1.18 and incidence of 10°, the flow pattern is very different from those in the subsonic cases. In Fig. 10 (c), the stream lines go through the cascade nearly smoothly. However, a small and thin separation region exists on the center part on the suction surface, where the stream lines deviate from the suction surface slightly. The separation region is clearly shown in the flow pattern on the suction surface in Fig. 13. Compared with the results of the subsonic cases above, the separation is pushed more downstream with its size shrunk. The flow is attached before the separation and re-attached after the separation. The reduced size of the separation may be due to the increased kinetic energy with higher inlet Mach number compared with the subsonic flow. The separation is mostly induced by the shock wave/turbulent boundary layer interaction. The same flow pattern is observed in the experimental visualization (Fig. 13) with the separation bubble size a little larger than that obtained in the computation.

There are two shock waves captured in the computation, the passage shock and lip shock as shown in Fig. 16. Compared with the experiment, the passage shock is located more upstream than the measured one. It is suspected that the computed boundary layer is predicted to be too thick and the excessive blockage pushes the shock more upstream. The local adverse pressure gradient caused by the shock wave/turbulent boundary layer interaction is the reason to

create the local separation shown in Fig. 13. In the experiment, there is a very weak trailing shock, which is not captured by the computation. Further numerical study is in progress to see if the better shock structure can be captured.

# 4 Conclusion

The separation phenomenon in a transonic flutter cascade under high incidence angle is numerically studied by solving the three-dimensional *Navier-Stokes* equations with *Baldwin-Lomax* turbulence model. The solver is validated using the turbulent flat plate boundary layer flow and a transonic inlet-diffuser flow. Several numerical cases with 2 incidence angles, 0°and 10° and 3 inlet *Mach* numbers, 0.5, 0.8 and 1.0 are computed. The following conclusions are drawn.

High incidence triggers the flow separation on the blade suction surface. At subsonic inlet Mach number 0.5 and 0.8, a large separation region is formed immediately from the leading edge when the incidence is increased from 0° to 10°. The inlet Mach number determines the characteristics of the separation region. When then inlet flow is subsonic, the size of the separation region increases with the inlet Mach number. This is evidenced as the separation region of Mach 0.8 is greater than that of Mach 0.5. The predicted separation flow pattern and the separation bubble length agree well with the experiment. The overall predicted surface pressure distribution agrees reasonably well with the experiment, except in the suction surface leading edge region where the computation predicts the pressure rise more steeply than that of the experiment.

When the inlet flow becomes supersonic, shock waves appear in the flow path close to the cascade leading edge. The shock wave/turbulent boundary layer interaction causes the flow separation, which is is pushed more downstream with smaller size compared with the case in subsonic.

# References


[1] B. S. Baldwin and H. Lomax. Thin layer approximation and algebraic model for separated turbulent flows. *AIAA Paper 78-257*, 1978.

[2] T. J. Bogar, M. Gajben, and J. C. Kroutil. Characteristic frequency and lengh scales in transonic diffuser flow oscillations. *AIAA Paper 81-1291*, 1981.

[3] Rodrick V. Chima, Eric R. McFarland, Jerry R. Wood, and Jan Lepicovsky. On flowfield periodicity in the NASA transonic flutter cascade, Part II–numerical study. Technical report NASA/TM–2000-209933, National Aeronautics and Space Administraion, Glenn Research Center, Cleveland, Ohio 44135, 2000.

[4] B. Van Leer. Towards the ultimate convservative difference scheme, III. *Jouranl of Computational Physics*, 23:263–75, 1977.

[5] J. Lepicovsky, R. V. Chima, T. A. Jett, T. J. Bencic, and K. E. Weiland. Investigation of flow separation in a transonic-fan linear cascade using visualization methods. *NASA/TM-2000-210521*, December 2000.

[6] J. Lepicovsky, E. R. McFarland, V. R. Capece, T. A. Jett, and R. G. Senyitko. Methodology of blade unsteady pressure measurement in the nasa transonic flutter cascade. *NASA/TM–2002-211894*, October 2002.

[7] J. Lepicovsky, E. R. McFarland, R. V. Chima, and J. R. Wood. On flowfield periodicity in the nasa transonic flutter cascade, part I — experimental study. *NASA/TM-2000-209934*, March 2000.

[8] P. Roe. Approximate riemann solvers, parameter vectors, and difference schemes. *Journal of Compuational Physics*, 43:357–72, 1981.

[9] B. van Leer. Flux-vector splitting for the Euler equations. *Lecture Note in Physics*, 170, 1982.


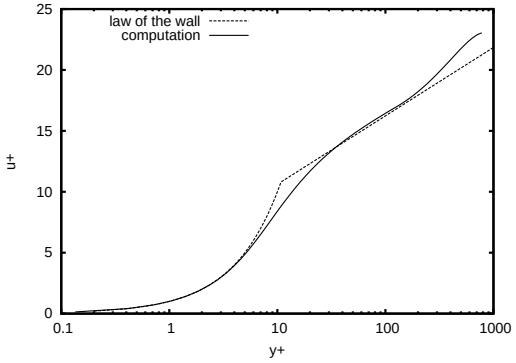


Figure 1: Computed velocity profile comparison with the law of the wall

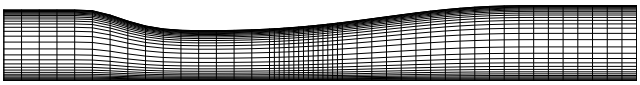

Figure 2: The transonic inlet-diffuser mesh

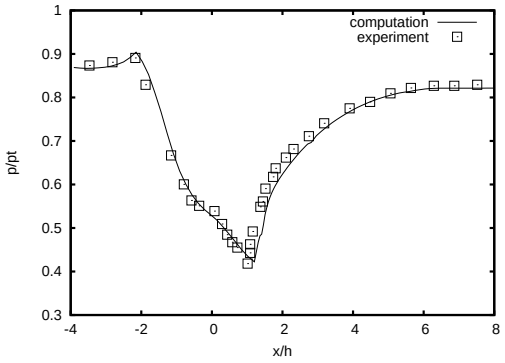


Figure 4: Upper wall pressure distribution of the transonic inlet-diffuser

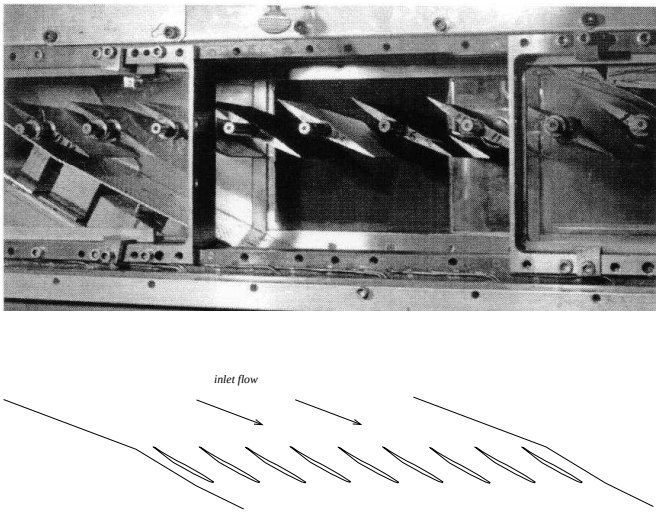


Figure 5: NASA transonic flutter cascade structure

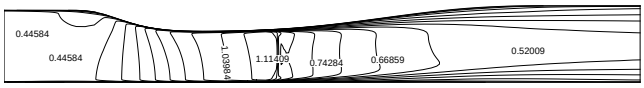


Figure 3: Mach number contours of the transonic inlet-diffuser

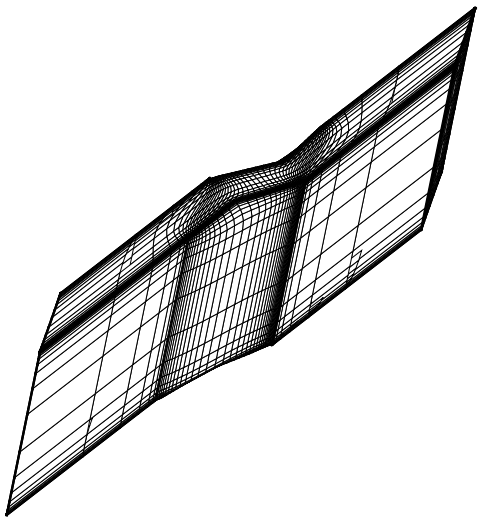

Figure 6: Cascade 3D mesh

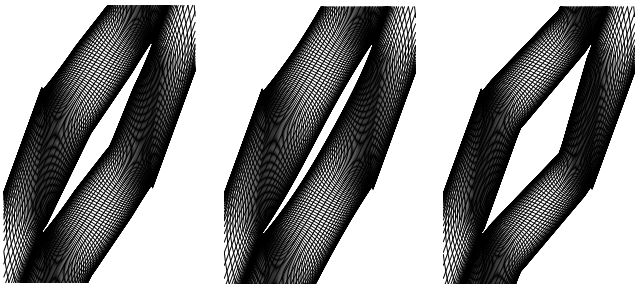

(a) bottom (b) midspan (c) top

Figure 7: Bottom, mid-span and top planes of the cascade mesh

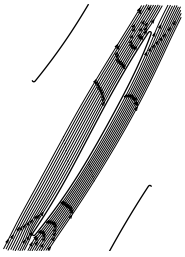

Figure 8: Flow pattern of the inlet-diffuser at incidence 0°

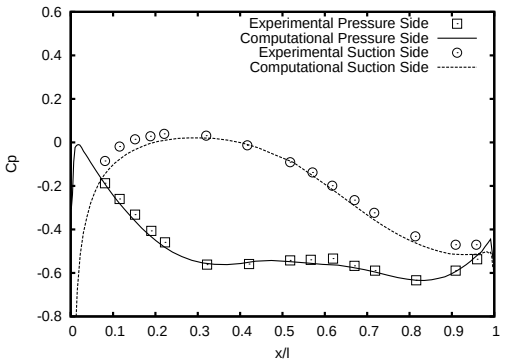


Figure 9: Mid-span static pressure distribution at Mach number 0.5

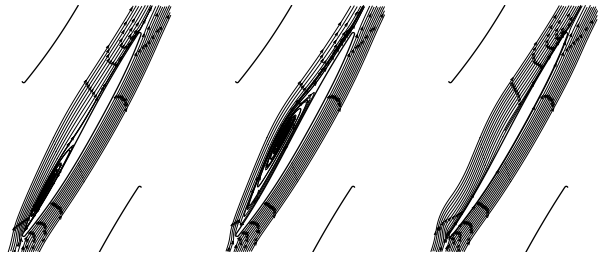

(a) Ma=0.5 (b) Ma=0.8 (c) Ma=1.18

Figure 10: Mid-span flow pattern under different inlet Mach numbers

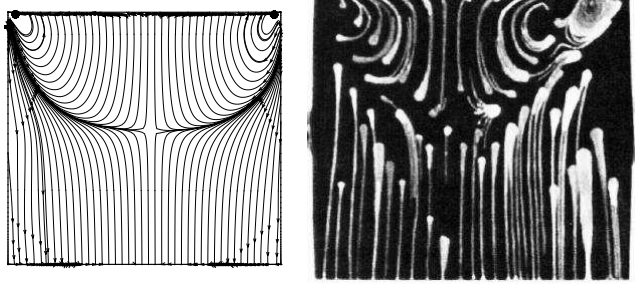

(a) Computated flow pattern (b) Experiment visualization

Figure 11: Suction surface flow pattern at Mach number 0.5

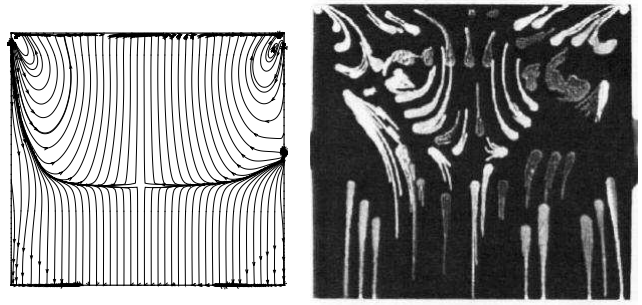

(a) Computated flow pattern (b) Experiment visualization

Figure 12: Suction surface flow pattern at Mach number 0.8

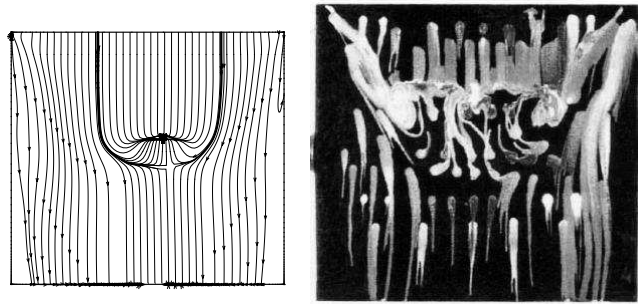

(a) Computated flow pattern (b) Experiment visualization

Figure 13: Suction surface flow pattern at Mach number 1.18

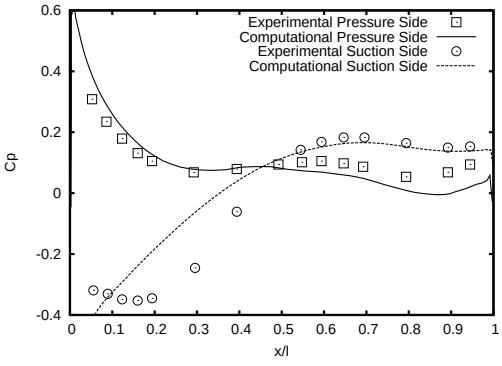


Figure 14: Mid-span static pressure distribution at Mach number 0.5

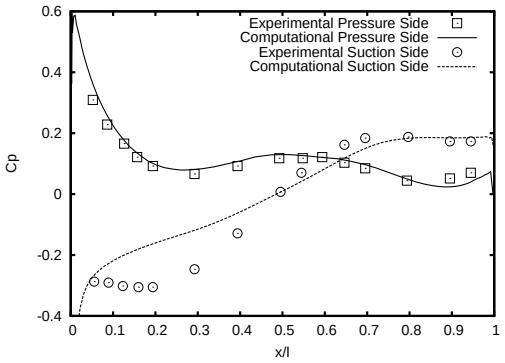


Figure 15: Mid-span static pressure distribution at Mach number 0.8

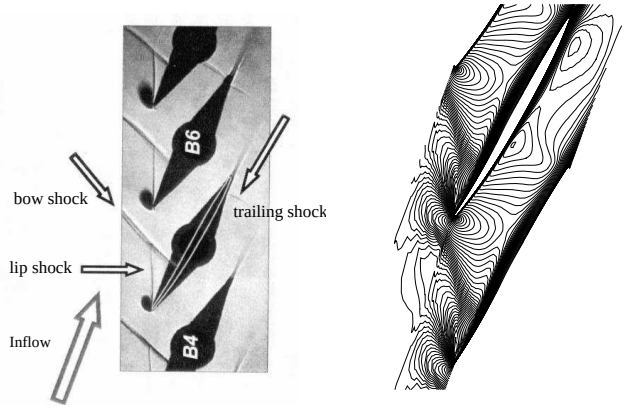


Figure 16: Experimental shock structure of the NASA transonic cascade at Mach number 1.18